

0017-9310(95)00062-3

Computational analysis of convection heat transfer to non-spherical particles

J. K. COMER and C. KLEINSTREUER†

Department of Mechanical and Aerospace Engineering, North Carolina State University, Raleigh,
NC 27695-7910, U.S.A.

(Received 9 May 1994 and in final form 30 January 1995)

Abstract—Steady laminar axisymmetric thermal flow past solitary oblate spheroids and non-spherical droplets at constant temperature has been numerically analysed. Mean Nusselt number correlations as a function of Reynolds number (i.e. $40 \leq Re \leq 120$), aspect ratio (i.e. $0.2 \leq E \leq 1.0$) and Prandtl number (i.e. $Pr = 0.7$ and 7.0) are presented for rigid spheroids. Non-sphericity effects of water and n-hexane fuel droplets on heat transfer mechanisms are also discussed. Thus, the analysis may form a base case for studying spheroidal particle effects in convection heat transfer systems.

INTRODUCTION

One of the key assumptions in dispersed flow simulations is that of particle sphericity. Thus, the extent to which the particle shape affects the interfacial transport properties is of basic interest. Specifically, considering steady laminar axisymmetric thermal flow past a rigid oblate spheroid or a non-spherical non-evaporating droplet, the gas phase convection heat transfer is analysed and mean Nusselt number correlations for spheroids of different aspect ratios are proposed. This base case study is of interest in a first-step analysis and design of a wide range of two-phase flows, including spray systems, air-breathing propulsion systems, separators, etc. Surface blowing due to droplet vaporization and transient effects such as vortex shedding, droplet oscillations and multiple droplet interactions, will be considered in future work.

Experimental observations and computational analyses indicate that the oblate spheroid is in many applications a good shape-approximation for non-spherical droplets [1, 2]. Furthermore, it is assumed that the particles are non-oscillating for the Reynolds number range of interest i.e. $40 \leq Re \leq 120$ [1]. Reviews of theoretical solutions and experimental correlations to low and intermediate Reynolds number flows past non-spherical axisymmetric solids have been given by Clift *et al.* [1], Happel and Brenner [3] and Soo [4]. Most notable are the numerical solutions of the reduced Navier–Stokes equations presented by Masliyah and Epstein [5, 6], Pitter *et al.* [7] and Chuchottaworn and Asano [8]. Masliyah and Epstein [5] performed an extensive numerical study of the flow field around both oblate and prolate spheroids with principle axis ratios of 1 to 0.2 for Reynolds numbers up to 100. In a complementary study, Masliyah and

Epstein [6] determined the heat and mass transfer quantities for rigid oblate and prolate spheroids with a principle axis ratio of 0.2. The analysis was limited to constant property flow at Reynolds numbers up to 100 with a Prandtl number of 0.7 and creeping flow at various Peclet numbers. Several Nusselt number correlations were presented. However, these correlations are not readily usable due to the required knowledge of the spheroidal surface area which is not easily calculated. Pitter *et al.* [7] studied the flow field around thin oblate spheroids with aspect ratios of 0.05 and 0.2 at intermediate Reynolds numbers. Their results compared well with the results by Masliyah and Epstein [5] as well as their own experimental observations. More recently, Chuchottaworn and Asano [8] performed an extensive numerical study of the flow characteristics as well as the transport phenomena associated with flow around both prolate and oblate rigid spheroids (labeled as ‘spheroidal droplets’ by the authors) over a wide range of aspect ratios. This analysis was limited to constant-property flow at intermediate Reynolds numbers with Prandtl/Schmidt numbers of 0.5 to 2.0. The results compared well with both Masliyah and Epstein [5, 6] and Pitter *et al.* [7]. Dwyer and Dandy [9] studied the fully *three-dimensional* thermal flow field which exists for rigid ellipsoids whose principle axes are not aligned with the flow. This work shows the effect of various angles of attack on the distribution of the surface pressure, shear stress and heat flux, as well as the mean Nusselt number and the drag coefficient.

Very little work has been done in the area of thermal flow past non-spherical *droplets*. A brief review of this topic has been given by Clift *et al.* [1]. The determination of the ‘true’ droplet shape result from flow-induced deformation is of prime importance in the analysis of the real interfacial transport properties. Wellek *et al.* [10] experimentally studied the shape of

† Author to whom correspondence should be addressed.

the work by Dandy and Leal [12], the characteristic diameter is chosen as the spherical volume equivalent diameter. Integral quantities such as the total drag coefficient and mean Nusselt number can be expressed using either d_{axis} or d_{equiv} , as given in equations (20) and (21).

The dimensionless continuous gas phase equations are:

$$\nabla \cdot \mathbf{u}_g = 0 \quad (1)$$

$$(\mathbf{u}_g \cdot \nabla) \mathbf{u}_g = -\nabla p_g + \frac{1}{Re_g} \nabla^2 \mathbf{u}_g \quad (2)$$

and

$$(\mathbf{u}_g \cdot \nabla) T_g = \frac{1}{Pe_g} \nabla^2 T_g \quad (3)$$

The dimensionless governing equations for the liquid phase are:

$$\nabla \cdot \mathbf{u}_l = 0 \quad (4)$$

and

$$(\mathbf{u}_l \cdot \nabla) \mathbf{u}_l = -\nabla p_l + \frac{1}{Re_l} \nabla^2 \mathbf{u}_l \quad (5)$$

where the dimensionless terms are defined as:

$$\begin{aligned} \mathbf{u} &= \mathbf{u}^*/U_\infty^*, \quad p_{g,l} = p_{g,l}^*/(\rho_{g,l}^* U_\infty^{*2}), \\ T &= (T^* - T_0^*)/(T_\infty^* - T_0^*), \quad \nabla = \nabla^* d^*, \\ Re_g &= \left(\frac{\rho_g^* U_\infty^* d^*}{\mu_g^*} \right), \quad Re_l = \left(\frac{\rho_l^* U_\infty^* d^*}{\mu_l^*} \right), \\ &\text{and } Pe_g = Re_g Pr. \quad (6a-g) \end{aligned}$$

The present system can be characterized by four independent dimensionless groups; the continuous gas phase Reynolds number, Re_g , the density ratio, $\zeta = (\rho_l^*/\rho_g^*)$, the viscosity ratio, $\lambda = (\mu_l^*/\mu_g^*)$ and the aspect ratio, $E = (b/a)$. For the steady-state droplet shapes of Dandy and Leal [12], the aspect ratio is replaced by the Weber number, $We = (U_\infty^{*2} d^* \rho_g^*/\gamma^*)$. The Weber number indicates the degree to which droplets will dynamically deform. For this study, however, the droplet shapes are fixed *a priori*, thus the Weber number (i.e. the surface tension) does not appear in the problem statement. The liquid-phase Reynolds number was not included as one of the independent parameters because it can be expressed in terms of the gas-phase Reynolds number, the density ratio and the viscosity ratio as $Re_l = (\zeta/\lambda) Re_g$.

The continuous gas-phase flow field, although an infinite medium, has been limited to a cylindrical domain (cf. Fig. 1). Based on trial-and-error runs, its extent is large enough to satisfy all boundary conditions.

The inlet boundary conditions are:

$$u = 1, \quad v = 0, \quad T = 1. \quad (7a-c)$$

Natural boundary conditions are specified at the outlet and top boundaries respectively:

$$\frac{\partial u}{\partial z} = \frac{\partial v}{\partial z} = \frac{\partial T}{\partial z} = 0 \quad (8a-c)$$

$$\frac{\partial u}{\partial r} = \frac{\partial v}{\partial r} = \frac{\partial T}{\partial r} = 0. \quad (9a-c)$$

Along the centerline (i.e. the axis of symmetry, $r = 0$) the boundary conditions are:

$$v = 0, \quad \frac{\partial u}{\partial r} = \frac{\partial T}{\partial r} = 0. \quad (10a-c)$$

The interfacial compatibility conditions are for the solid particles:

$$u = v = 0, \quad T = 0 \quad (11a-c)$$

and for the droplets:

$$u_{n,g} = u_{n,l} = 0, \quad u_{t,g} = u_{t,l}, \quad \tau_{s,g}^* = \tau_{s,l}^*, \quad T = 0 \quad (12a-e)$$

where the shear stresses are defined as:

$$\tau_{s,g}^* = \tau_{s,g} \cdot (U_\infty^{*2} \rho_g^*) = \left(\frac{1}{Re_g} \cdot \frac{\partial u_t}{\partial n} \Big|_{r=R(z)} \right) \cdot (U_\infty^{*2} \rho_g^*) \quad (13a)$$

and

$$\tau_{s,l}^* = \tau_{s,l} \cdot (U_\infty^{*2} \rho_l^*) = \left(\frac{1}{Re_l} \cdot \frac{\partial u_t}{\partial n} \Big|_{r=R(z)} \right) \cdot (U_\infty^{*2} \rho_l^*). \quad (13b)$$

In non-dimensional form the continuity of shear stress is written as:

$$\tau_{s,l} = \left(\frac{\rho_g^*}{\rho_l^*} \right) \tau_{s,g} = \left(\frac{1}{\zeta} \right) \tau_{s,g}. \quad (14)$$

The interfacial quantities such as separation angle, pressure distribution, drag coefficient and Nusselt number, are calculated for all cases. The drag coefficient is comprised of two components: the form (i.e. pressure) drag coefficient and the skin (i.e. friction) drag coefficient

$$C_{D_{\text{Total}}} = C_{D_{\text{Form}}} + C_{D_{\text{Skin}}} \quad (15a)$$

where

$$C_{D_{\text{Form}}} = \left(\frac{8}{\pi \cdot d^2} \right) \int_0^\pi (\sigma_n)_z dA \quad (15b)$$

$$C_{D_{\text{Skin}}} = \left(\frac{8}{\pi \cdot d^2} \right) \int_0^\pi (\tau_{s,g})_z dA. \quad (15c)$$

The shear stress, $\tau_{s,g}$, is defined by equation (13a) and the normal stress is given below:

$$\sigma_n^* = \sigma_n (U_\infty^{*2} \rho_g^*) = \left(-p + \frac{2}{Re_g} \cdot \frac{\partial u_n}{\partial n} \Big|_{r=R(z)} \right) (U_\infty^{*2} \rho_g^*). \quad (16)$$

The Nusselt number, $Nu_d = (h^* d^*/k^*)$, can be related to the non-dimensional surface heat flux, q_s'' , which in

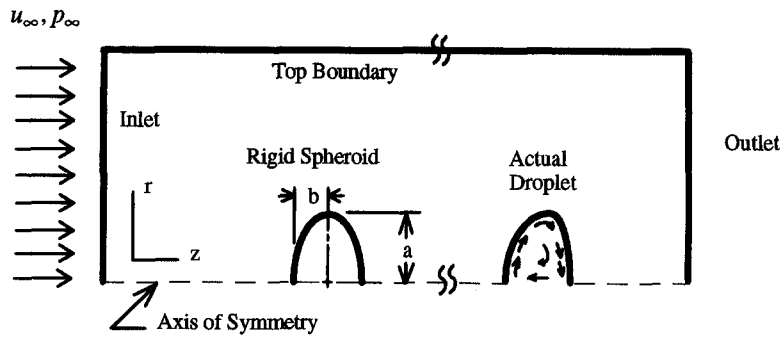


Fig. 1. System schematic.

turn is directly proportional to the non-dimensional temperature gradient at the interface.

$$Nu_d = Pe q_s'' = - \frac{\partial T}{\partial n} \tag{17}$$

Here, the non-dimensional heat flux is defined as:

$$q_s'' = \frac{q_s^*}{[\rho_g^* c_p^* U_\infty^* (T_\infty^* - T_0^*)]} \tag{18}$$

The Nusselt number and the non-dimensional surface heat flux are by definition always positive quantities, while the temperature gradient is always a negative quantity. This is easily verified from the definition of the non-dimensional temperature, equation (6c), which is based on the fact that the normal direction always points away from the interface.

The analysis involving both solid and liquid oblate spheroids is based on a characteristic length equal to a spheroid's major principle axis. This choice of characteristic length is suitable for the analysis of solid particles of varying aspect ratios, as well as for the comparison between liquids and solids of the same aspect ratio. However, this choice of characteristic length does not allow comparisons between droplets of different aspect ratios. Droplets of different aspect ratios correspond to droplets of different volumes. Thus employing $d = d_{axis}$ provides little insight into the effect of droplet deformation on the continuous phase thermal flow field or the dispersed phase isothermal flow field. Therefore, the calculated results were transformed to correspond to a characteristic length equal to the spherical volume equivalent diameter. Reynolds numbers, drag coefficients and Nusselt numbers based on a characteristic length equal to the spheroid's major principle axis can be transformed to correspond to an equivalent spherical-volume system as follows:

$$Re_{dc} = Re_{da}(E)^{1/3} \tag{19}$$

$$C_{D_{dc}} = C_{D_{da}} \left(\frac{1}{E} \right)^{2/3} \tag{20}$$

$$Nu_{d_{dc}} = Nu_{d_{da}}(E)^{1/3} \tag{21}$$

where

$d_e \in$ volume equivalent diameter, d_{equiv} .

$d_a \in$ major principal axis, d_{axis} .

NUMERICAL SOLUTION

In the Galerkin finite-element formulation a system of nonlinear algebraic equations of the form

$$[S]\mathbf{v} + [N(\mathbf{v})]\mathbf{v} + \varepsilon^{-1}[L]^u[D]^{-1}[L]\mathbf{v} = \mathbf{F} \tag{22}$$

appears [16]. Linearization of equation (22) is obtained with the efficient quasi-Newton method if the radius of convergence is sufficient [16]. For problems with small computational domains (i.e. the liquid droplet domain) the fully coupled penalty formulation of (22) is used. Instead of solving the *global* system matrix found in (22), the gas phase quantities are obtained with a *segregated* solver algorithm using the 'mixed' formulation where each conservation equation is solved separately [17]. Hence, for large problems, creation of a huge global matrix is avoided in favor of a group of smaller sub-matrices which are solved in a sequential order. Due to the sequential nature of this algorithm, more iterations are required than for the fully-coupled method; however, the time per iteration may be short so that for very large problems a significant reduction in both computer time and core memory requirements may result.

The dimensions of the computational domain depend primarily on the free stream velocity, the fluid Prandtl number, and the particle shape (cf. Fig. 2). The radial dimension is inversely related to the aspect ratio and the Peclet number and the axial dimensions are directly related to the Peclet number and inversely related to the aspect ratio. A variable-density meshing strategy is utilized where small elements are placed at the interface and smoothly transitioned to coarser elements at the boundaries. The nodal spacing on the interface is about 3.2 degrees for $E = 1$, i.e. a sphere. Nine-node isoparametric quadrilateral elements were used where the velocity and temperature were approximated by biquadratic shape functions and the pressure by linear shape functions [16]. Meshes for spheroidal particles were generated by multiplying the sphere's streamwise axis by the aspect ratio. The mesh

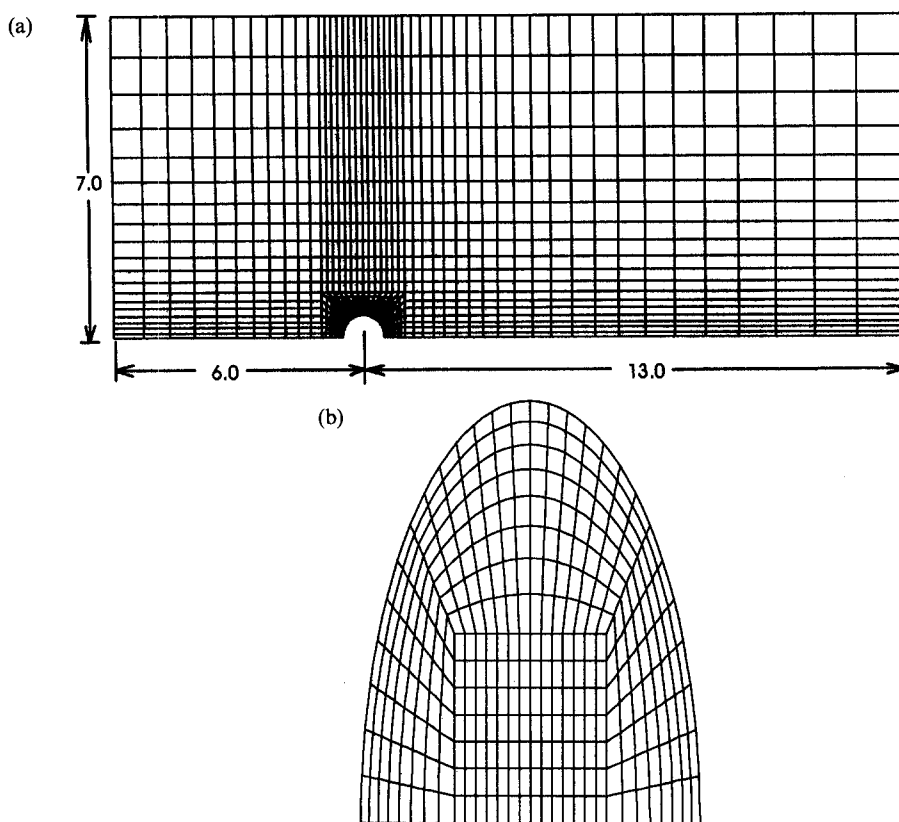


Fig. 2. (a) Representative finite-element mesh for axisymmetric flow past spherical/non-spherical particles and drops. (b) Liquid-phase mesh for a spheroidal droplet, $E = 0.4$.

was refined and skewness of elements near the interface was reduced for the worst case, i.e. a spheroid with aspect ratio $E = 0.2$, until mesh-independence of the results was achieved. About 1020–1325 elements were needed for the gas phase and 322–350 elements were necessary for the droplets.

The software utilized (cf. ref. [17]) was directly applicable to the single-phase problem (i.e. thermal flow past rigid spheroids). However, the direct extension to the two-phase droplet flow problem, while possible, was found to be neither computationally efficient nor stable. The liquid droplet domain is subject to Neumann boundary conditions, requiring a slow and robust iteration scheme, while the larger gas phase domain is subject to Dirichlet boundary conditions, which allow for quicker, less robust schemes. If both phases are solved simultaneously, the slower more robust scheme required for the droplet region must be used for the 'entire' domain. For this reason, the two domains were solved sequentially utilizing the aforementioned software package in combination with a supplemental interfacial convergence routine. The solution procedure for the gas and liquid flow fields was obtained as follows. Starting with Stokes' flow for the gas phase as an initial guess, the interface is considered first to be rigid. The resulting shear stress at the interface is used as the boundary condition for the liquid phase. The stress-induced

liquid-phase flow field is solved and the surface velocity is used as the interfacial boundary condition for the gas phase. The matching of the compatibility conditions required between nine and 30 iterations with an optimal under-relaxation coefficient of 0.65 and a maximum relative error bound of 10^{-3} . Higher Reynolds number flows utilize the lower Reynolds number solution as their initial guess.

RESULTS AND DISCUSSION

The finite-element software used (cf. ref. [17]) has been validated with empirical correlations for fluid flow and heat transfer parameters presented by Clift *et al.* [1]. Table 1 summarizes the comparisons for solid spheres while Fig. 3 shows a comparison of the local Nusselt number for air flow at $Re = 100$ past a solid particle with aspect ratios $E = 1.0$ and 0.2 . Chiang [18], Comer [19] and Comer and Kleinstuever [20] provide additional tables and graphs comparing numerical predictions and accepted data sets for thermal flow past liquid spheres and solid spheroids. Table 1 shows a very good agreement between the predicted flow data and empirical correlations while the corresponding Nusselt number data sets differ slightly for Peclet numbers greater than, say, 500. The discrepancies may be caused in part by complications in measuring indirectly the Nusselt number for higher

Table 1. Comparison of data sets for rigid sphere

Re	Separation angle, θ_s		Drag coefficient, C_D		Nusselt no., Nu_m ($Pr = 0.7$)		Nusselt no., Nu_m ($Pr = 7.0$)	
	Model	Clift [1]	Model	Clift [1]	Model	Clift [1]	Model	Clift [1]
40	143.9	144.4	1.80	1.79	5.007	5.077	9.655	9.691
50	138.9	139.3	1.58	1.57	5.398	5.457	10.516	10.521
60	135.3	135.5	1.43	1.42	5.749	5.795	11.303	11.259
75	131.4	131.4	1.27	1.26	6.220	6.247	12.403	12.240
90	128.4	128.2	1.15	1.14	6.644	6.648	13.425	13.111
100	126.6	126.5	1.09	1.09	6.906	6.894	14.060	13.645
110	125.2	125.0	1.04	1.04	7.158	7.126	14.673	14.148
120	123.8	123.7	1.00	0.99	7.400	7.347	15.256	14.625

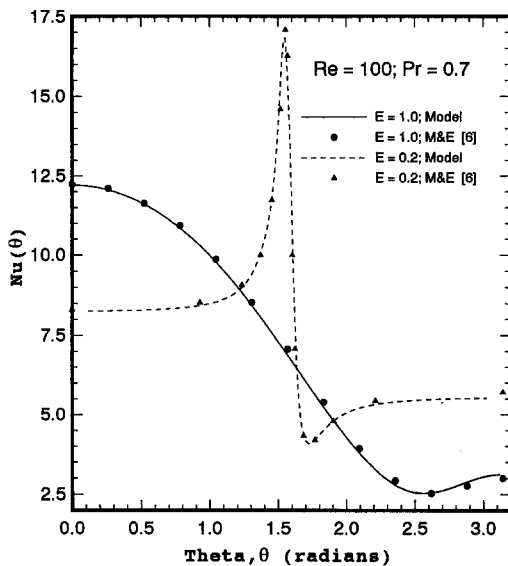


Fig. 3. Local Nusselt number variations for rigid oblate spheroids compared with those presented by Masliyah and Epstein [6].

Prandtl number fluids which exhibit much thinner *thermal* boundary layers. On the other hand, mesh refinement for accurate simulation also has some practical limits, especially in the interfacial high-curvature region of non-spherical particles.

A. Solid spheroids

Figures 4(a) and 4(b) depict the effects of aspect ratio (i.e. $E = 0.4-1.0$) and gas stream velocity (i.e. $Re_{da} = 40$ and 120 for $Pr = 0.7$) on the local Nusselt number of solid spheroids. It is observed that at the stagnation point, $\theta = 0^\circ$, the magnitude of $Nu(\theta = 0^\circ)$ varies directly with E . As can be deduced from the Reynolds analogy, as the frictional drag coefficient decreases with smaller aspect ratios the Nusselt number reduces for a given Peclet number. In contrast, at the rear stagnation point, $\theta = 180^\circ$, the Nusselt number is almost independent of the aspect ratio if the Peclet number is small (cf. Fig. 4(a)). However,

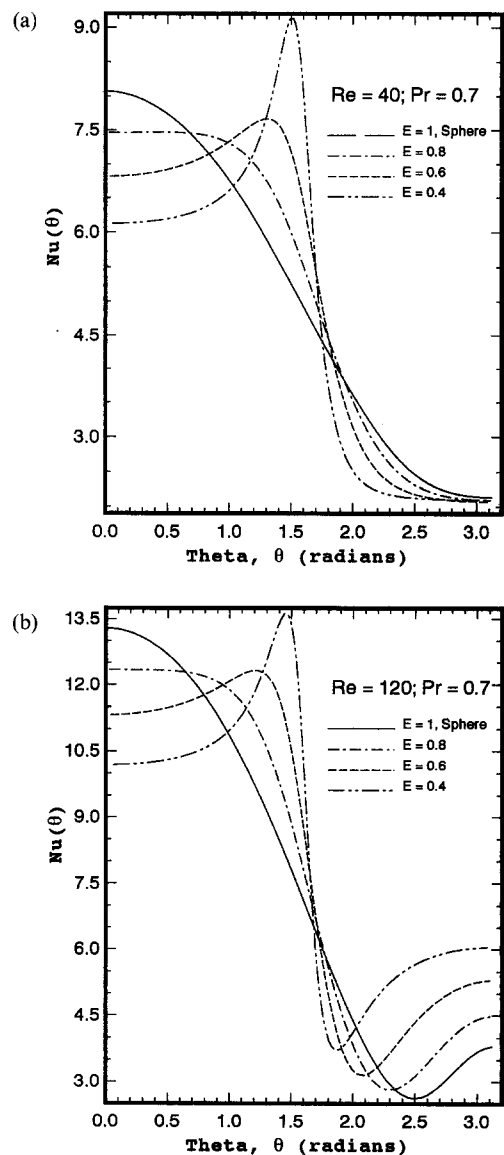


Fig. 4. Local Nusselt number variation for aspect ratios $E = 1, 0.8, 0.6, 0.4$; (a) at $Re = 40$ and $Pr = 0.7$; (b) at $Re = 120$ and $Pr = 0.7$.

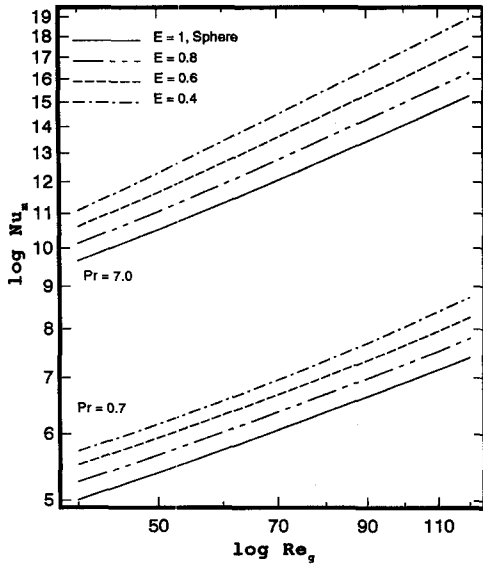


Fig. 5. Mean Nusselt number for $Pr = 0.7, 7.0$ and aspect ratios $E = 1, 0.8, 0.6, 0.4$.

with increasing Peclet numbers, wake recirculation effects generate recoveries of the local Nusselt numbers which increase as the aspect ratio decreases (cf. Fig. 4(b)). These local (instantaneous) Nusselt numbers are most important when simulating multiple interacting vaporizing droplets. When plotting the surface-averaged Nusselt numbers $Nu_m = Nu_m(Re, Pr, E)$ on a log-log graph (cf. Fig. 5), two heat transfer correlations for $Pr = 0.7$ and $Pr = 7.0$ at intermediate Reynolds numbers were obtained via least-squares curve fitting.

$$Nu_m = 1.393 Re_{da}^{0.348} \exp[0.248(1-E)] \quad \text{for } Pr = 0.7 \quad (23a)$$

$$Nu_m = 2.074 Re_{da}^{0.415} \exp[0.31(1-E)] \quad \text{for } Pr = 7.0. \quad (23b)$$

The major advantage of these two correlations is their ease of use. The differently weighted influence of the Reynolds number in the two equations is due to the approximation of the *nonlinear* effect of the Prandtl number on the heat transfer, employing a *linear* coefficient.

B. Non-spherical droplets

In the light of the *isothermal* droplet assumption, the major difference in convection heat transfer between droplets and solids is caused by the shear stress induced (surface) motion of the liquid phase. This in turn influences the thermal gas boundary layer, the interface temperature gradient and hence the Nusselt number (cf. equation (17)). The velocity and isotherm plots depicted in Figs. 6 and 7 show the effects of the viscosity and aspect ratios on the gas phase velocity and temperature fields at $Re_{da} = 100$. The viscosity and aspect ratio effects on the liquid phase

flow field are given in ref. [20]. It can be seen that the higher viscosity water droplet has a larger (i.e. more robust) recirculation zone than the lower viscosity n-hexane droplet, whose wake region is almost stagnant. As a result, the isotherms are closer together near the rear stagnation point for the water droplet than for the n-hexane droplet, which indicates that water droplets have a higher heat transfer rate in this region. However, light fuel droplets have substantially higher heat transfer rates over the front part because of increased droplet circulation which results in higher overall Nusselt numbers. When comparing droplets with different aspect ratios it is important to remember that the characteristic diameter, and hence the Reynolds number, used in this analysis was based on the major principle axis. Hence, the actual volume-equivalent Reynolds number for the case $E = 0.4$ is $Re_{de} \approx 75$ (cf. Fig. 7). Thus for the same volume-equivalent Reynolds number the effect of the aspect ratio on the recirculation zone and the corresponding isotherms would be even more pronounced. For water droplets with $\lambda = 40.2$, $Nu_{m,liquid}$ differs only marginally from $Nu_{m,solid}$ for intermediate Reynolds numbers and for all aspect ratios because of the significantly reduced slip velocities (cf. Fig. 8). In contrast, for liquids with low viscosity ratios, for example n-hexane fuel droplets with $\lambda = 4.12$, $Nu_{m,liquid}(Re)$ differs substantially from $Nu_{m,solid}(Re)$ as shown in Fig. 9. When using the volume-equivalent diameter as a length scale, as would be appropriate for comparisons between deforming but non-evaporating droplets of differing aspect ratios, $Nu_{m,liquid}$ is approximately independent of the aspect ratio in the range $0.5 \leq E \leq 1.0$ [19]. However, the rate of heat transfer is by no means independent of the aspect ratio. In fact the rate of heat transfer increases as the aspect ratio decreases, since the surface area of a spheroid is inversely proportional to the aspect ratio.

The gas phase velocity vector and constant-temperature fields for steady-state (i.e. equilibrium) droplet shapes corresponding to $We = 0.5$ and 8.0 [2] are depicted in Figs. 10(a) and 10(b) respectively. The effects of the Reynolds and Weber numbers on the liquid phase flow field are shown in refs. [2] and [12]. By comparing the graphs, it is evident that the droplet corresponding to $We = 8.0$ has a larger principle axis than the droplet corresponding to $We = 0.5$ (cf. Fig. 10). This is because the characteristic diameter used in this analysis was equal to the volume equivalent diameter (i.e. the volume was held constant while the droplet deformed). It can be seen that the droplet corresponding to $We = 0.5$ is essentially spherical and the velocity and temperature fields resemble those shown in Fig. 6(b). At $We = 8.0$ the droplet is nearly spheroidal and approaches a shape similar to Fig. 7(b) (i.e. $E \approx 0.4$). As was the case for solid spheroids (cf. Fig. 4), the local Nusselt number in the vicinity of the frontal stagnation point is directly related to the aspect ratio. Thus the local Nusselt number over the front of the $We = 0.5$ droplet is larger than that over the

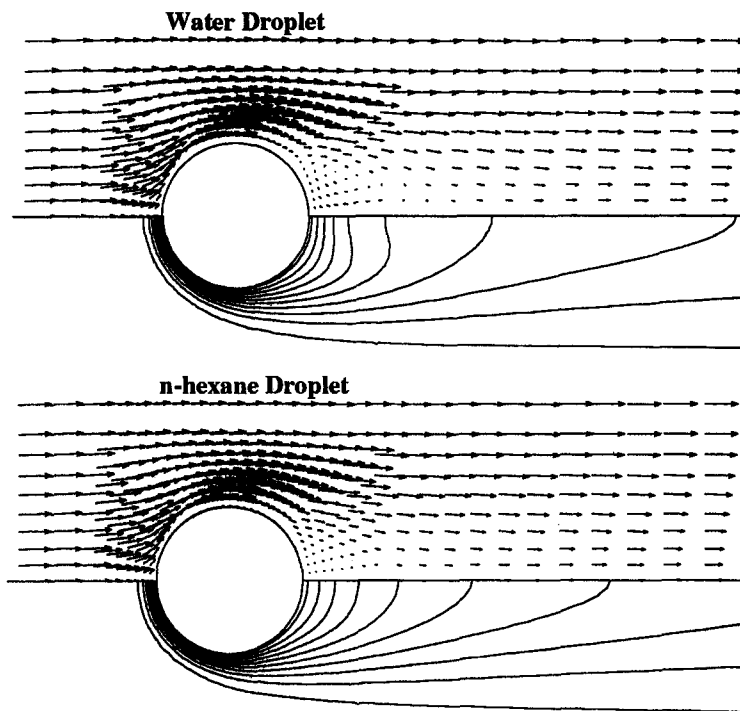


Fig. 6. Velocity and isotherms for spherical water ($\lambda = 40.2$ and $\zeta = 845.6$) and n-hexane ($\lambda = 4.12$ and $\zeta = 260.7$) droplets where $E = 1$, $Re = 100$ and $Pr = 0.7$.

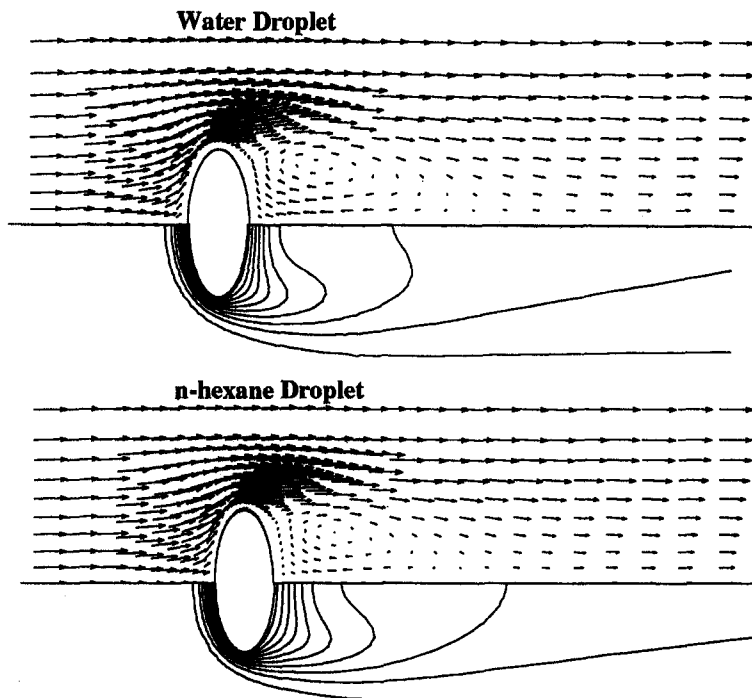


Fig. 7. Velocity and isotherms for spheroidal water ($\lambda = 40.2$ and $\zeta = 845.6$) and n-hexane ($\lambda = 4.12$ and $\zeta = 260.7$) droplets where $E = 0.4$, $Re = 100$ and $Pr = 0.7$.

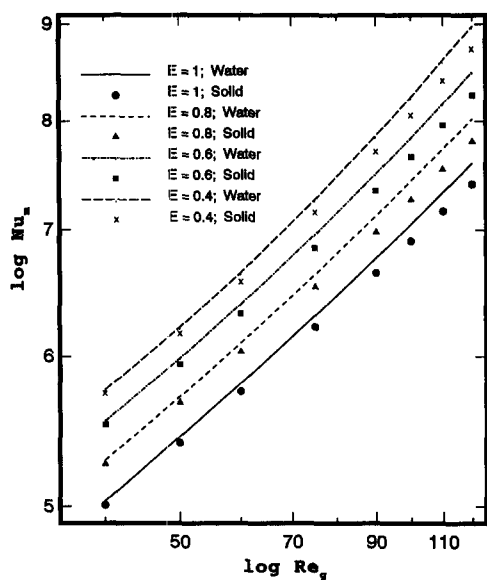


Fig. 8. Mean Nusselt number based on the principal axis for a water droplet ($\lambda = 40.2$ and $\zeta = 845.6$) and a rigid oblate spheroid at aspect ratios, $E = 1, 0.8, 0.6, 0.4$ for a $Pr = 0.7$.

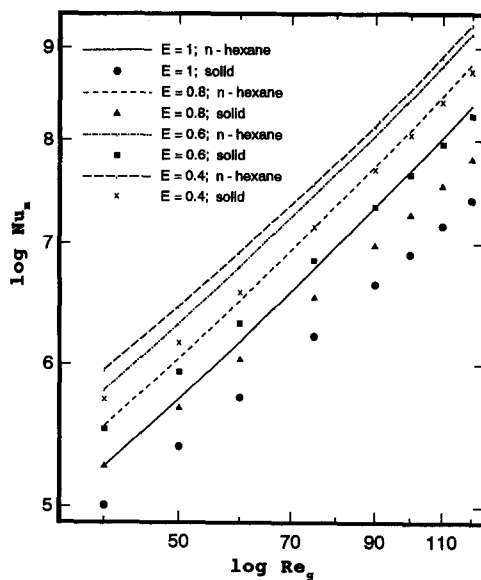


Fig. 9. Mean Nusselt number based on the principal axis for an n-hexane droplet ($\lambda = 4.12$ and $\zeta = 260.7$) and a rigid oblate spheroid at aspect ratios, $E = 1, 0.8, 0.6, 0.4$ for a $Pr = 0.7$.

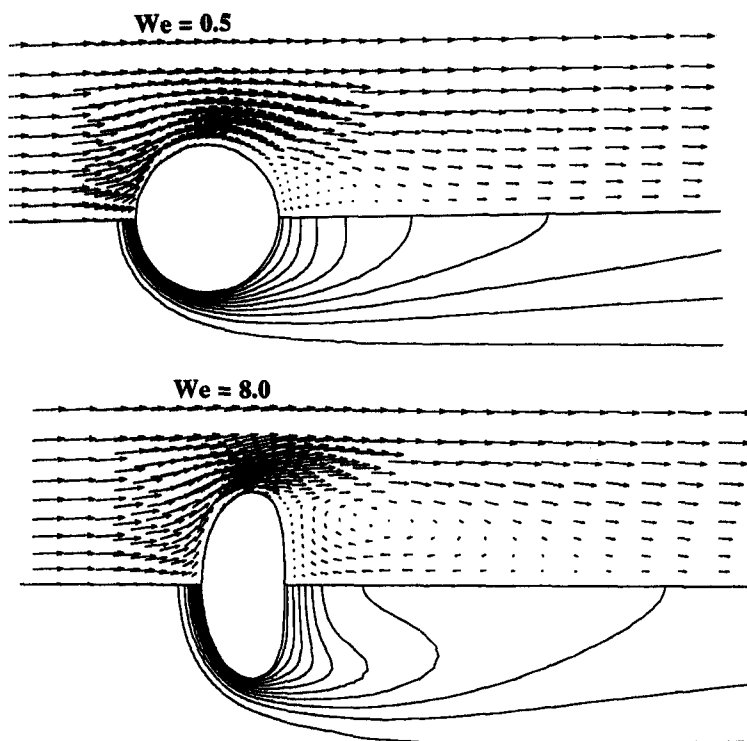


Fig. 10. Velocity and isotherms for the steady-state droplet shapes of Dandy [2] for ($\lambda = 4, \zeta = 0.909, We = 0.5$ and 8.0) at $Re = 100, Pr = 0.7$.

$We = 8.0$ droplet. The $We = 8.0$ droplet has a much larger and stronger recirculation region; however, the isotherm spacings appear to be approximately the same for both droplets near the rear stagnation point, indicating equivalent local Nusselt numbers in this region. The mean Nusselt numbers for the dynam-

cally deformed droplet shapes are shown in Fig. 11. The droplet corresponding to $We = 8.0$ has a lower Nusselt number and heat flux than does the droplet with $We = 0.5$ as alluded to above. However, the deformed droplet has a higher overall heat transfer rate since it has substantially more surface area than

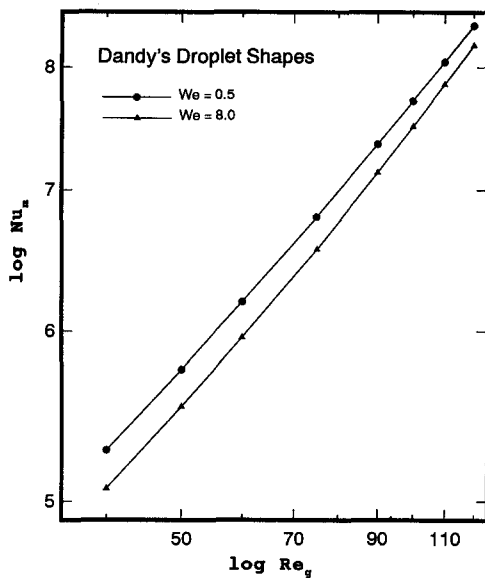


Fig. 11. Mean Nusselt number based on the volume equivalent diameter for the liquid droplet shapes calculated by Dandy [2] for $We = 0.5$ and 8.0 ($\lambda = 4$ and $\zeta = 0.909$ and $Re = 60$) for $Pr = 0.7$.

the spherical droplet. The close agreements between the equilibrium shapes (cf. Fig. 10) and the spheroidal shapes (cf. Figs. 6 and 7) support the present assumption that most deformed droplets can be modeled as spheroids.

Acknowledgment—This work was supported in part by the Computational Science Graduate Fellowship Program of the Office of Scientific Computing in the Department of Energy.

REFERENCES

1. R. Clift, J. R. Grace and M. E. Weber, *Bubbles, Drops and Particles*, Chap. 2, pp. 5–7. Academic Press, New York (1978).
2. D. S. Dandy, Intermediate Reynolds number free stream flows, Ph.D. Thesis, Caltech, Pasadena, CA (1987).
3. J. Happel and H. Brenner, *Low Reynolds Number Hydrodynamics*, Chap. 4, p. 5. Prentice-Hall, New Jersey (1965).
4. S. L. Soo, *Multi-phase Fluid Dynamics*, Chap. 2. Science Press, Beijing, P.R.C. and Gower Technical, Brookfield, USA (1990).
5. J. H. Masliyah and N. Epstein, Numerical study of steady flow past spheroids, *J. Fluid Mech.* **44**, 493–512 (1970).
6. J. H. Masliyah and N. Epstein, Numerical solution of heat and mass transfer from spheroids in steady axisymmetric flow, *Prog. Heat Mass Transfer* **6**, 613–632 (1972).
7. R. L. Pitter, H. R. Pruppacher and A. E. Hamielec, A numerical study of viscous flow past a thin oblate spheroid at low and intermediate Reynolds numbers, *J. Atmos. Sci.* **30**, 125–134 (1973).
8. P. Chuchottaworn and K. Asano, Numerical analysis of drag coefficients and the heat and mass transfer of spheroidal drops, *J. Chem. Engng Jap.* **19**, 208–213 (1986).
9. H. A. Dwyer and D. S. Dandy, Some influences of particle shape on drag and heat transfer, *Phys. Fluids A*, **2**, 2110–2118 (1990).
10. R. M. Wellek, A. K. Agrawal and A. H. P. Skelland, Shape of liquid drops moving in liquid media, *A.I.Ch.E. J.* **12**, 854–862 (1966).
11. J. D. Taylor and A. J. Acrivos, On the deformation and drag of a falling viscous drop at low Reynolds number, *J. Fluid Mech.* **18**, 466–476 (1964).
12. D. S. Dandy and L. G. Leal, Buoyancy-driven motion of a deformable drop through a quiescent liquid at intermediate Reynolds numbers, *J. Fluid Mech.* **208**, 161–192 (1989).
13. C. Kleinstreuer and H. Chiang, Convection heat transfer of closely-spaced spheres with surface blowing, *Wärme Stoffübertragung* **28**, 285–293 (1993).
14. C. Kleinstreuer, J. K. Comer and H. Chiang, Fluid dynamics and heat transfer with phase change of multiple spherical droplets in a laminar axisymmetric gas stream, *Int. J. Heat Fluid Flow* **14**, 292–300 (1993).
15. H. Chiang and C. Kleinstreuer, Computational analysis of interacting vaporizing fuel droplets on a one-dimensional trajectory, *Combust. Sci. Technol.* **86**, 289–309 (1992).
16. C. Cuvelier, A. Segal and A. A. Van Steenhoven, *Finite Element Methods and Navier-Stokes Equations*, Chaps 4, 7, 8. Reidel, Dordrecht (1986).
17. M. S. Engleman, *FIDAP Manual*, Vol. 1, Theoretical Section, Chap. 7. FDI, Evanston, IL (1991).
18. H. Chiang, Numerical analysis of interacting spheres and vaporizing droplets, Ph.D. Thesis, North Carolina State University, Raleigh, NC (1991).
19. J. K. Comer, Computational analysis of thermal flow past non-spherical solids and droplets, M.S. Thesis, North Carolina State University, Raleigh, NC (1993).
20. J. K. Comer and C. Kleinstreuer, A numerical investigation of laminar flow past non-spherical solids and droplets, *ASME J. Fluids Engng* **117**, 170–175 (1995).